Research Article | Vol. 30, No. 16 / 1 Aug 2022 / Optics Express 28290
Optics EXPRESS

Axial accuracy in localization microscopy with 3D point spread function engineering

MARIJN E. SIEMONS,[1,3] LUKAS C. KAPITEIN,[1] AND SJOERD STALLINGA[2,4]

[1]Cell Biology, Neurobiology and Biophysics, Department of Biology, Utrecht University, The Netherlands
[2]Department of Imaging Physics, Delft University of Technology, The Netherlands
[3]marijnsiemons@gmail.com
[4]s.stallinga@tudelft.nl

Abstract: Single-molecule localization microscopy has developed into a widely used technique to overcome the diffraction limit and enables 3D localization of single-emitters with nanometer precision. A widely used method to enable 3D encoding is to use a cylindrical lens or a phase mask to engineer the point spread function (PSF). The performance of these PSFs is often assessed by comparing the precision they achieve, ignoring accuracy. Nonetheless, accurate localization is required in many applications, such as multi-plane imaging, measuring and modelling of physical processes based on volumetric data, and 3D particle averaging. However, there are PSF model mismatches in the localization schemes due to how reference PSFs are obtained, look-up-tables are created, or spots are fitted. Currently there is little insight in how these model mismatches give rise to systematic axial localization errors, how large these errors are, and how to mitigate them. In this theoretical and simulation work we use a vector PSF model, which incorporates super-critical angle fluorescence (SAF) and the appropriate aplanatic correction factor, to analyze the errors in z-localization. We introduce theory for defining the focal plane in SAF conditions and analyze the predicted axial errors for an astigmatic PSF, double-helix PSF, and saddle-point PSF. These simulations indicate that the absolute axial biases can be as large as 140 nm, 250 nm, and 120 nm for the astigmatic, saddle-point, and double-helix PSF respectively, with relative errors of more than 50%. Finally, we discuss potential experimental methods to verify these findings and propose a workflow to mitigate these effects.

1. Introduction

Single-molecule localization microscopy (SMLM) [1–3] is a super-resolution microscopy modality that overcomes the diffraction limit by localization of sparse emitting fluorophores. The lateral position of a single-molecule is estimated from a blinking event by fitting the spot with a 2D Gaussian which resembles an ideal unmodified point spread function (PSF). More advanced SMLM implementations modify or engineer the PSF to encode for other parameters of interest, such as the z-position [4], emission wavelength [5] or orientation [6]. The most common way for z-encoding in 3D SMLM is the use of PSF engineering by a cylindrical lens for astigmatic z-encoding. Other popular engineered PSFs are the double-helix PSF (DH-PSF) [7–9] and TetraPod [10] or saddle-point PSF (SP-PSF) [11]. For 3D SMLM with PSF engineering, a calibration PSF is obtained by scanning a small fluorescent bead with a z-stage over a suitable range. This calibration PSF is then used to create a look-up-table (LUT) [4], a cubic spline model [12], or used as input to create a PSF with a scalar model used for direct fitting [11] or for training a neural network [13].

However, the calibration PSF is obtained by acquiring a through focus scan of a small fiducial marker by moving the z-stage. This stage-movement PSF differs from the PSF a fluorophore would exhibit with different z-positions inside the sample while the z-stage remains static. This results in a different defocus aberration and therefore a different PSF. Moreover, often high NA

#461750 https://doi.org/10.1364/OE.461750
Journal © 2022 Received 29 Apr 2022; revised 29 May 2022; accepted 9 Jun 2022; published 18 Jul 2022

Optics EXPRESS

TIRF objectives are used which capture the super-critical angle fluorescence (SAF) alongside the under-critical angle fluorescence (UAF). The SAF depends strongly on the absolute distance from the cover slip, following an exponential falloff within ~ 1 wavelength, resulting in a strong z-dependent apodization in the pupil. The through-focus calibration PSF therefore differs in SAF and defocus aberration from the "true" PSF of an emitter as a function of depth inside the sample. Current implementations using engineered PSFs either do not make such a distinction between calibration and emitter PSF or use simplified PSF models. These simplified PSF models are either scalar, don't include SAF or Fresnel reflections, don't use the correct aplanatic correction factor, or ignore a combination of these effects.

Another method to estimate the z-position of the fluorophore is to measure the ratio between the UAF and SAF [14–16]. This method enables accurate z-position estimation but can only be used close to the cover slip (< 500 nm) and requires a complicated set-up. Therefore the currently most popular method for 3D localization is astigmatic PSF engineering, which can be easily implemented by inserting a cylindrical lens at the emission port of the microscope.

Most assessments of localization method performance focus on the best possible precision, as quantified by the Cramér-Rao lower bound, while little attention is paid to accuracy, the absence of bias in the parameter estimation. In some cases inaccurate 3D SMLM is sufficient to gain basic insight, but accurate z-localization is important in many biological cases and studies. It is crucial to have accurate 3D information when the super-resolution volume is used for the modelling of physical processes and forces, for instance in focal adhesion sites [17] or neuronal synapses [18]. This is especially the case when these 3D nano-organizations can be correlated to other measurable quantities, such as action potentials [19] or diffusion [20,21]. Axial accuracy is also important for multi-plane SMLM [22,23], where multiple focal planes have to be stitched together. Lastly, accurate localization is important in 3D particle averaging, where even small relative axial biases are noticeable, as these methods can achieve resolutions down to 10 nm [24].

To date, z-accuracy in 3D SMLM has not been quantified or explored in great detail, but there have been attempts to address this issue. Recently proposed experimental calibration methods use a sample with fluorescent beads embedded in a gel or on top of polymer coating in order to create LUTs at different depths [25,26]. However, the method by Li *et al*. [25] can only be applied for astigmatic PSFs and relates the LUTs with respect to the position when a bead is in focus by stage movement. There is therefore a mismatch between the LUT and the emitter PSF. The calibration method proposed by Petrov and Moerner [26] does not have these pitfalls as the imaging depth is well defined and arbitrary PSFs can be used. However, in that case the PSF is acquired by stage-movement, which again induces a mismatch between the calibration PSF and the true emitter PSF.

For that reason there is a need for accurate z-localization with PSF engineering and, in general, insight in how large these axial errors are. In this theory and simulation work we use a vector PSF model, which includes SAF and the appropriate aplanatic correction factor, to analyze the accuracy in z-localization. We introduce theory for defining the plane of best focus in SAF conditions and analyze the predicted axial errors for an astigmatic PSF, DH-PSF and SP-PSF. Finally we discuss potential experimental methods to verify these findings and propose a workflow to mitigate these effects.

2. Theory

2.1. Vector PSF model

A vector PSF model that includes Fresnel coefficients has been described in earlier work [27]. In short, the rotation matrix $\mathbf{R}(\vec{\rho})$ describes how the x, y, and z-component of the emitted electric field $\mathbf{E}^{\text{object}}$ in the object plane are transferred by the objective lens (see Fig. 1(b)) to the electric field in the pupil plane $\mathbf{E}^{\text{pupil}}$

$$\mathbf{E}^{\text{pupil}}(\vec{\rho}) = \mathbf{R}(\vec{\rho})\mathbf{E}^{\text{object}}(\vec{\rho}) \tag{1}$$

Optics EXPRESS

with $\vec{\rho} = (\rho_x, \rho_y)$ the normalized pupil coordinates, shown in Fig. 1(a). The z-component of the electric field in the pupil is ignored, as this component gives a contribution to the spot focused by the tube lens on the camera that scales with the square of the (low) NA of the tube lens, which can therefore be neglected. The 6 components of the electric field at the pupil with (additional) phase aberration $W(\vec{\rho})$ are given by

$$\begin{aligned} E_{l,j}^{\text{pupil}}(W, \vec{\rho}) &= \frac{1}{w_n} A q_{l,j} \exp\left[iW(\vec{\rho})\right] \\ &= \frac{1}{w_n} A q_{l,j} \exp\left[iW_{\text{eng}}(\vec{\rho}) + i(dk_z^1 - z_{\text{stage}} k_z^3 - z_{\text{pos}} k_z^\alpha)\right] \end{aligned} \tag{2}$$

with $W_{\text{eng}}(\vec{\rho})$ the phase corresponding to the engineered PSF, $q_{l,j}$ the polarization vector component that includes the Fresnel-coefficients for the interfaces between the different media (sample, cover slip, immersion oil) with refractive index n_α. The definitions of $q_{l,j}$ and the Fresnel-coefficients can be found in Ref. [27], Eqs. (4)–(7). $\vec{k}$ is the wave-vector with $k_{x/y} = 2\pi \text{NA} \rho_{x/y}/\lambda$ and $k_z^\alpha = 2\pi\sqrt{n_\alpha^2 - \text{NA}^2\rho^2}/\lambda$, with $\alpha = 1$ for the mounting medium and $\alpha = 3$ for the immersion oil. d is the distance between the coverslip and the focal plane inside the sample, z_{stage} denotes the corresponding z-stage position with that focal plane, and z_{pos} is the difference of the emitter with respect to the focal plane either by movement of the stage ($k_z^\alpha = k_z^3$) or movement inside the mounting medium ($k_z^\alpha = k_z^1$) and w_n is a normalized factor. We refer to Fig. 2(a) for an illustration for the definitions of the relevant axial positions. In the case of movement inside the mounting medium, z_{pos} needs to be smaller than the imaging depth d to have a physically meaningful result. A is a correction factor for imaging with a refractive index medium mismatch and is given by

$$A(\rho) = \sqrt{\frac{n_{\text{imm}} \cos(\theta_{\text{imm}})}{n_{\text{med}} \cos(\theta_{\text{med}})}} \frac{1}{\sqrt{n_{\text{med}} \cos(\theta_{\text{med}})}} = \frac{\left(n_{\text{imm}}^2 - \text{NA}^2\rho^2\right)^{1/4}}{\left(n_{\text{med}}^2 - \text{NA}^2\rho^2\right)^{1/2}} \tag{3}$$

where the factor $\sqrt{n_{\text{imm}} \cos(\theta_{\text{imm}}) / n_{\text{med}} \cos(\theta_{\text{med}})}$ corrects for the wave compression between the mounting medium – glass – immersion oil interface and the factor $1/\sqrt{n_{\text{med}} \cos(\theta_{\text{med}})}$ is the aplanatic amplitude correction factor. Here $\theta_{\text{med/imm}}$ denotes the angle of a light ray in the mounting medium or immersion oil corresponding to the scaled polar coordinate $\rho = n_\alpha \sin(\theta_\alpha)$.

The incoherent PSF H, arising from emission from a dipole that experiences no orientational constraint and rotates quickly compared to the exposure time, is then computed by quadratically adding the 6 Fourier transforms of the electric field components in the pupil

$$H(x, y) = \frac{N}{3} \sum_{l=x,y} \sum_{j=x,y,z} \left| \int_{|\rho^2|<1} E_{l,j}^{\text{pupil}} \exp\left[-i(k_x x + k_y y)\right] d^2\rho \right|^2 \tag{4}$$

with N the number of photons emitted. To illustrate the effects of high NA imaging on the PSF we compared this to a scalar model. This scalar model has the same correction factor A and includes Fresnel-coefficients in order to include the SAF (see Figs. 1(c),(d) for the amplitude and the phase of the electric field). The comparison of the two models (see Figs. 1(e),(f)) shows that the scalar model significantly deviates from the vector model and exhibits more interference fringes. The vector PSF does not resemble an Airy disk, but is more akin to a Gaussian with a shoulder.

2.2. Focal plane in SAF conditions

In order to quantify axial biases it is important to define the focal plane of the microscope. The plane of best focus of an imaging system is commonly defined as the plane where the

Optics EXPRESS

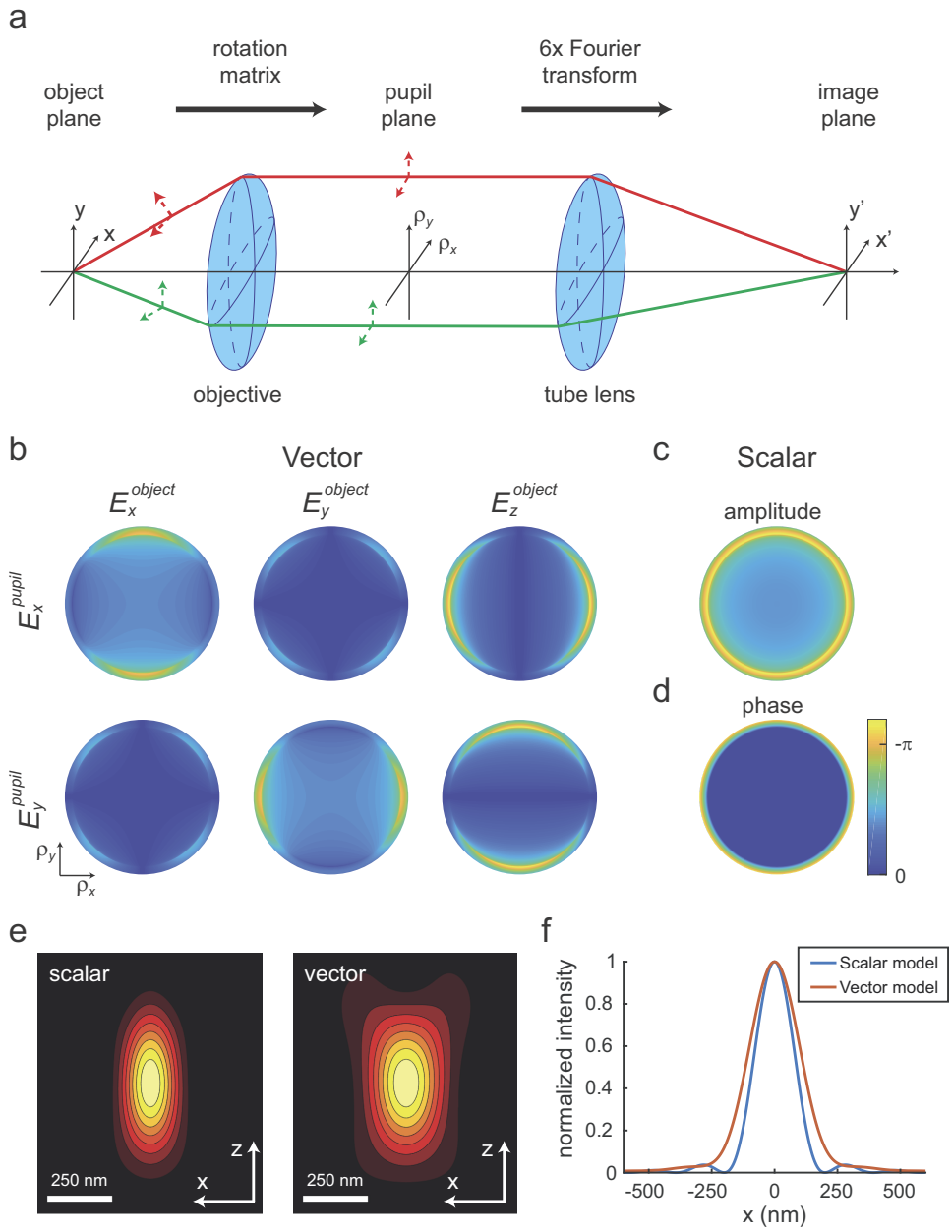

Fig. 1. Illustration of the vector PSF model and the difference with a scalar PSF model. (a) The electric field emitted at the object plane is rotated by the objective lens to the pupil plane, resulting in 6 electric field components in the pupil plane. The electric field in the image plane is computed by a Fourier transform. (b) The amplitude of the 6 components of the electric field in the pupil plane for an emitter at the coverslip (d = 0 nm) with a TIRF objective (1.49 NA, λ = 550 nm, n_1 = 1.33, $n_2 = n_3$ = 1.52). Plots are shown with normalized pupil coordinates ranging [−1, 1]. (c),(d) The amplitude (c) and phase (d) of the electric field in the case of a scalar model. (e) Scalar and vector PSF of the models shown in (b) and (c),(d) with stage movement. (f) Comparison of the scalar and vector PSF model in focus.

Optics EXPRESS

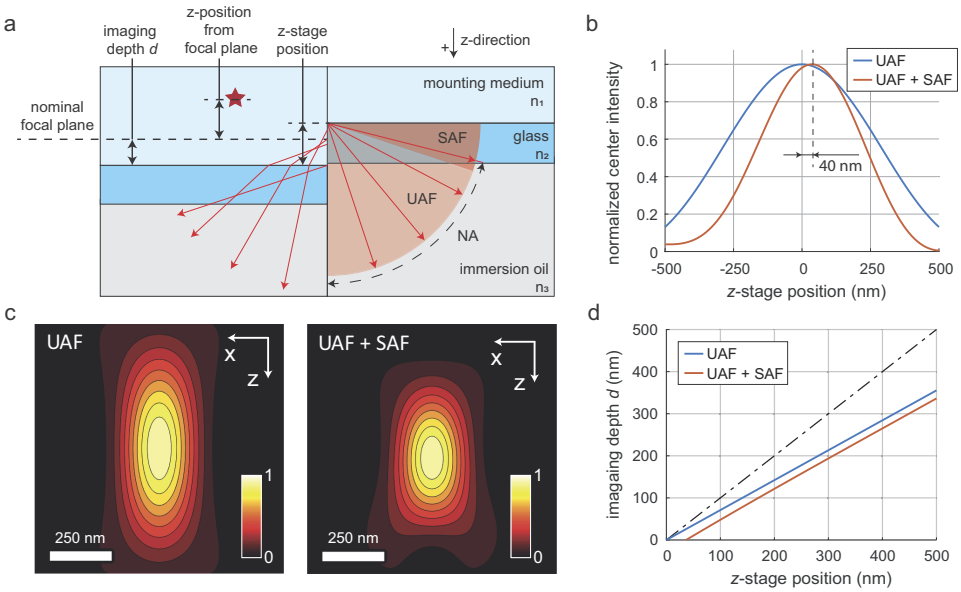

Fig. 2. Effect of super-critical angle fluorescence (SAF) on the focal plane. (a) Illustration of the definitions in this work. (b) The maximum intensity occurs at a z-stage position of 40 nm when the SAF is included. (c) Comparison between the PSF with only under-critical angle fluorescence (UAF) and in the case of UAF and SAF. The latter exhibits a more compact PSF and is axially asymmetric. (d) The imaging depth d as function of the z-stage position.

root-mean-square wave-front distortion W_{rms} is minimal [28]. However, when imaging in a condition with a strong apodization in the pupil plane, not all aberrations contribute equally to the PSF. To incorporate both the amplitude and phase variations across the pupil, we propose an optimization metric based on the Strehl ratio to find the actual focal plane. The optimal z-stage position corresponding to a focal plane with an imaging depth d from the cover slip (see Fig. 2(a)) according to this metric can be found by

$$\max_{z_{\text{stage}}} S\left(W_{\text{eng}} + dk_z^1 - z_{\text{stage}}k_z^3, W_{\text{eng}}\right) \tag{5}$$

where we define the relative Strehl-ratio $S(W_1, W_2)$ as

$$S(W_1, W_2) = \frac{\sum_{l=x,y} \sum_{j=x,y,z} \left| \int_{|\rho^2|<1} d^2\rho E_{l,j}^{\text{pupil}}(W_1) \right|^2}{\sum_{l=x,y} \sum_{j=x,y,z} \left| \int_{|\rho^2|<1} d^2\rho E_{l,j}^{\text{pupil}}(W_2) \right|^2}. \tag{6}$$

We implemented this optimization scheme by computing this ratio over a range of z-positions near an initial estimated value ($z_{\text{stage}} = dn_3/n_1$). The optimum is found by fitting a second order polynomial around the maximum value. The results of this procedure are shown in Fig. 2(b).

This analysis reveals that for focusing an dipole that has an average emission over the exposure time that is isotropic, the optimal z-stage position deviates 40 nm from zero. To illustrate that this effect is purely caused by the SAF we simulated a PSF with z-stage movement with only UAF (NA = 1.33) and UAF + SAF (NA = 1.49) as shown in Fig. 2. The UAF PSF is symmetric around the focal plane, whereas the focal plane for the SAF + UAF PSF is shifted and the PSF

Optics EXPRESS

appears asymmetric. Therefore, the z-stage needs to be adjusted to reduce the phase difference between the SAF and the UAF for optimal focusing. As expected, the difference between the SAF+UAF and UAF actual focus planes reduces when focusing deeper into the sample as shown in Fig. 2(d).

It turns out that optimizing the proposed relative Strehl ratio for finding the actual focus plane only works when the phase for PSF engineering is small compared to the wavelength ($W_{\mathrm{rms}}<0.1\lambda$) and does not contain a phase singularity in the centre. The procedure maximizes the intensity at the center of the PSF. Therefore this method can find the correct focal plane in the case of an astigmatic PSF, but fails to find the focal plane in the case of a SP or DH PSF because these do not contain the maximum intensity in the center of the PSF in focus. To find the focal plane in these cases the PSF engineering phase should be disregarded during the optimization, except modes which affect the focal plane position (i.e., Zernike modes with azimuthal order of 0 such as Z_2^0, Z_4^0, etc.).

3. Simulation results

We next explored the effect of the SAF and spherical aberration on z-encoding for three types of engineered PSFs: an astigmatic PSF, a SP-PSF, and a DH-PSF. So far we examined the PSF when the z-stage is moved. However, during a SMLM experiment the z-stage remains fixed, while emitters have a different position with respect to the focal plane. This change in position has a different associated z-component of the wave-vector as well as a z-position dependent apodization due to the SAF. The calibration PSF acquired by moving the z-stage is therefore inherently different than the true PSF that represents the 3D position inside the mounting medium. In the following we term the PSF obtained by movement of the z-stage at zero imaging depth "stage-movement PSF" and the true emitter PSF representing 3D position inside the mounting medium "emitter PSF". This corresponds to a multiplication of the z-position with the z-component of the wave-vector in either immersion oil (k_z^3) or mounting medium (k_z^1) respectively [Eq. (2)]. All simulations are, unless specified differently, carried out with the following parameters: λ = 550 nm, pixel size = 100 nm, NA = 1.49, n_{med} = 1.33, and n_{imm} = 1.52. We have simulated the error in the estimated z-position when not correcting for these differences in axial wave-vector components and examine the absolute error in z-position as well as the relative error, the derivative of the absolute error.

3.1. Astigmatic z-encoding

For the case of astigmatic z-encoding we simulated a calibration PSF of a small bead on the cover slip (imaging depth = 0 nm) with stage-movement and compared this to the emitter PSFs at three imaging depths (250, 500, and 750 nm), see Fig. 3. The stage-movement PSF has an almost axially symmetric ellipticity (Fig. 3(a)), resulting in a linear LUT as shown in Fig. 3(b). In contrast, the emitter PSF with an imaging depth of 250 nm exhibits large deviations from a 2D Gaussian function near the cover slip. This effect reduces for larger imaging depths (500 and 750 nm), but deviations from the LUT now occur away from the cover slip (negative z-positions) caused by spherical aberration and the reduction of the effective NA caused by the diminishing SAF. Using the calibration LUT for z-localization of the estimated width ratios result in underestimation of the true z-position up to 140 nm (56%). Furthermore, the relative axial errors range between 0.3 nm and 0.5 nm per nm distance over a range of hundreds of nanometers, see Fig. 3(d). This implies that medium sized structures of 100 nm can already accumulate up to 50% of relative axial error.

Optics EXPRESS

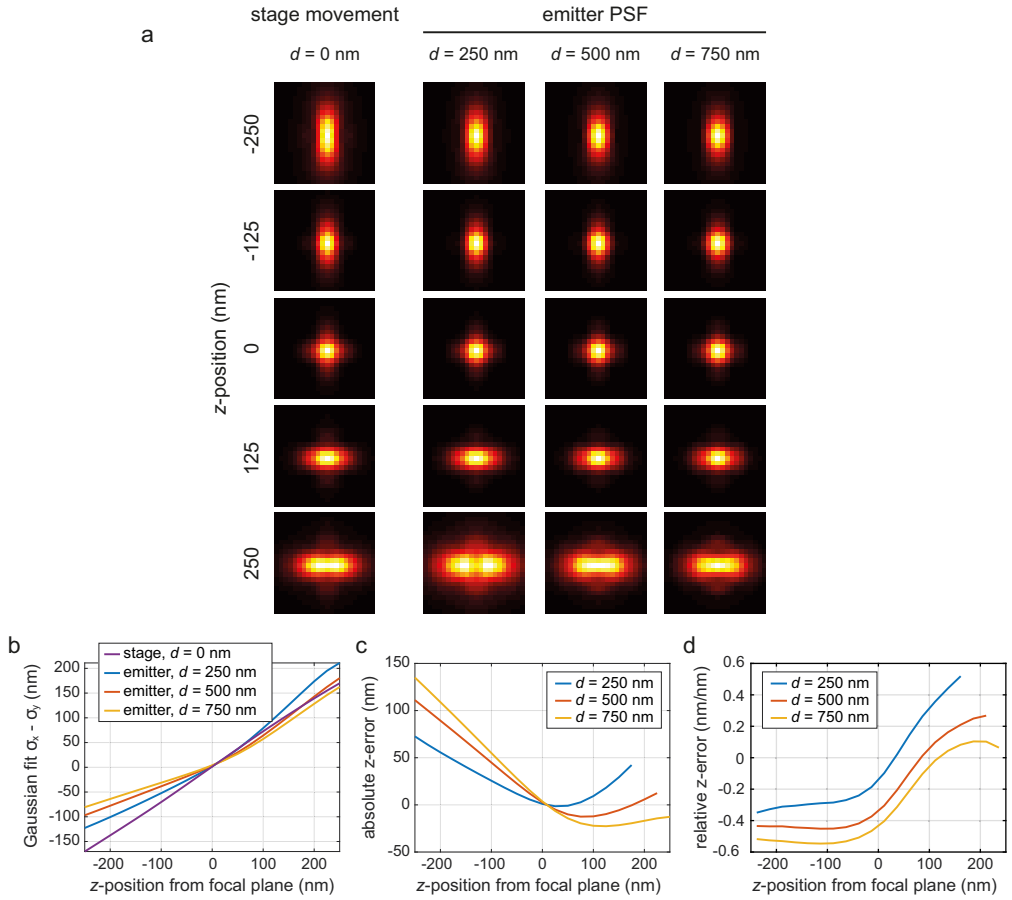

Fig. 3. (a) Astigmatic PSF with an astigmatism level of 60 nm (rms amplitude) with stage-movement at an imaging depth of 0 nm (left) and different axial position with respect to the focal plane for imaging depths of 250, 500, and 750 nm (right). (b) LUTs of the PSFs of (a) by Gaussian fitting. (c) Absolute z-error when using a LUT of the stage movement PSF for estimating the z-position at different imaging depths. (d) Relative axial error of (c) in nm error per nm distance.

Optics EXPRESS

3.2. Saddle-point and double-helix PSF

We made similar analyses for the SP and DH PSFs, optimized for an axial range of 1500 nm. We simulated the stage-movement PSF and compared this to the emitter PSF with an imaging depth of 750 nm and z-range of ±750 nm.

We will first discuss the SP PSF. We engineered the SP-PSF with Zernike modes Z_2^2 and Z_4^2 with amplitude 150 mλ and −148 mλ respectively (rms amplitude), values that were obtained by CRLB optimization. The phase of this SP-PSF is shown in Fig. 4(a). The stage-movement PSF deviates in a visually striking way from the emitter PSF as shown in Fig. 4(b). The emitter PSF exhibits a different pattern in the focal plane and has differently structured lobes in the extreme z-positions. To quantify the axial accuracy we simulated N = 100 noisy emitter PSFs per z-position with 2500 signal photon counts and 10 background photon counts per pixel and fitted these with the calibration PSF model. Figure 4(c) shows the fitted z-position as function of the true axial position. The z-accuracy appears to be non-linear over the axial range and deviates strongly close to the coverslip (<500nm). Strikingly, this analysis predicts absolute z-errors of more than 250 nm. Around focus, the relative error is about 0.5 nm/nm over a 500 nm range, which would result in a 250 nm sized structure to be overestimated by 125 nm.

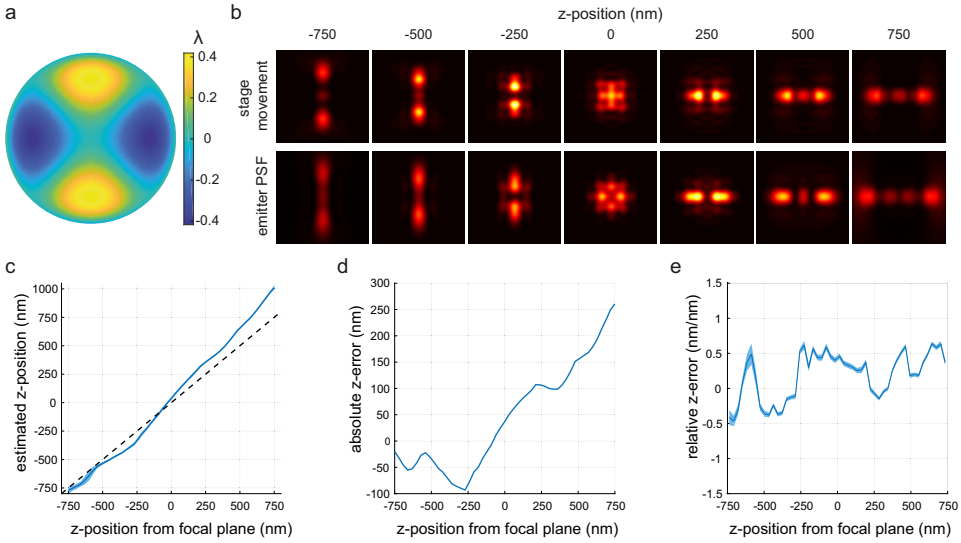

Fig. 4. (a) Phase profile of the SP PSF. (b) Stage-movement PSF at an imaging depth of 0 nm (top) and emitter PSF (bottom) at an imaging depth of 750 nm. Z-position denotes either the movement with the stage or position inside the mounting medium. Pixel size = 10 nm. (c) Estimated z-position for the SP PSF using the stage-movement PSF model to fit the true emitter PSF. Colored region indicates standard deviation of the estimated positions. (d) Absolute axial error of (c). (e) Relative axial error of (c). Shaded region indicates standard error of the mean.

We next explored the accuracy for the DH PSF. There are two popular ways to construct this PSF; using Gaussian-Laguerre modes [7] or using rings of azimuthal ramps [8,9]. Here we engineered the DH-PSF with 3 rings of azimuthal ramps with increasing slope with a ring radius ratio α of 4/5 resulting in a 2π rotation in 1500 nm. The phase of this PSF is shown in Fig. 5(a).

In the case of the DH-PSF there were no striking visual differences when comparing the stage-movement PSF and emitter PSF (see Fig. 5(b)), but there was a noticeable difference in the angle between the lobes. We measured the axial accuracy by analyzing the angle between the position of the maximum intensity of the two lobes as function of the z-position. Figure 5(c)

Optics EXPRESS

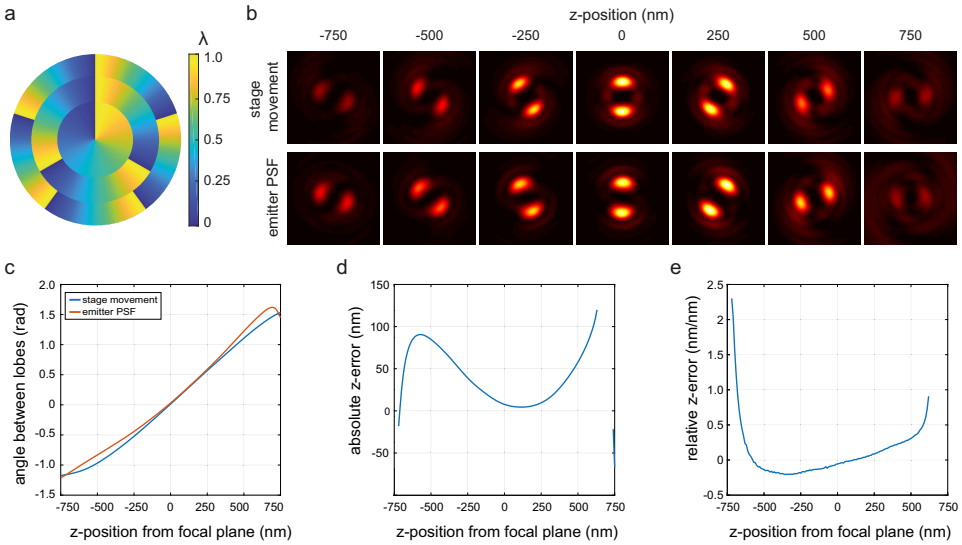

Fig. 5. (a) Phase profile of the DH PSF. (b) Stage-movement PSF at an imaging depth of 0 nm (top) and emitter PSF (bottom) at an imaging depth of 750 nm. Z-position denotes either the movement with the stage or position inside the mounting medium. Pixel size = 10 nm. (c) Angle between the two lobes for the stage-movement and emitter PSF. (d) Absolute axial error of (c). (e) Relative axial error.

shows that the angle of the emitter PSF deviates from the stage movement PSF and even rotates outside the calibration range near the coverslip. The largest measured absolute axial error is 120 nm, which is similar to the astigmatic PSF, but this axial error is accumulated over a larger z-range. The relative error for this DH-PSF is small compared to both the astigmatic PSF and SP-PSF, especially near the focus plane (±250 nm). The DH-PSF is therefore the most accurate form of PSF engineering out of these three PSFs.

4. Discussion

Despite the need for accurate axial localization to extend the usability of 3D SMLM, this topic has not yet been studied in great detail. The simulations performed in this work show that using the calibration PSF acquired by stage movement results in significant biases in the estimated z-position when performing 3D SMLM. These biases result from apodization in the pupil due to super-critical angle fluorescence and spherical aberration induced by the mismatch between immersion oil and the mounting medium. This leads to sizeable inaccuracies in z, which can amount to absolute z-errors of more than 140 nm in the case of an astigmatic PSF, 250 nm in the case of SP-PSF, and 120 nm in the case of DH-PSF. The relative z-errors with an astigmatic PSF and SP-PSF differ across the z-range but can be as large as 50% over ranges of tenths to hundreds of nanometers. Therefore, relative axial errors can accumulate to 50 nm or more. When using PSFs engineered for larger axial ranges, axial biases can possibly accumulate up to hundreds of nanometers. These simulations furthermore indicate that the DH-PSF has the best axial accuracy, especially in a ±250 nm range around the focal plane. This is in line with other work analyzing aberration sensitivity [29,30].

The specific contributions of the spherical aberration and SAF to the axial biases cannot be decoupled using this model because both effects arise from the refractive index mismatch between the mounting medium and the coverslip/immersion oil. Even far away from the coverslip where SAF is minimal (> wavelength), axial biases can still be introduced by SAF because the

Optics EXPRESS

calibration PSF (stage-movement PSF) is acquired in SAF conditions. Therefore, for accurate axial localization both effects need to be taken into account. It also points to the practical importance of avoiding or accurately characterizing the refractive index mismatch.

The substantial biases predicted by this model can be experimentally verified in a number of ways. One option is to use a large coated spherical surface, where the axial position can be derived from the lateral position [31]. It is important that the refractive index of the bead matches with the mounting medium in order to reduce aberrations introduced by the bead. Polystyrene beads with a high refractive index ($n = 1.7$) will therefore likely introduce aberrations as the fluorescence is collected partially through the bead. Another verification method is to use a setup which uses the ratio of the UAF and UAF + SAF to accurately measure the axial position while simultaneously measure the engineered PSF in a third channel. A downside of this method that it only works within a few wavelengths of the coverslip. Nonetheless, with such an approach it would be possible to verify a substantial part of the predictions in this work.

If these findings are indeed experimentally verified, all these effects can in principle be mitigated by fitting the spots directly with the vector PSF model. However, due to the complexity of this model, this is slow compared to other fitting algorithms. We therefore propose to use the following work flow (see Fig. 6). First a calibration PSF is acquired using a bead on the cover slip in the sample. Next a vector PSF based phase retrieval algorithm is used to estimate the aberrations precisely and accurately. This phase is then used to compute the emitter PSF for a certain z-stage position. This emitter PSF can then be used to create a LUT, a cubic spline model or train a neural network for fitting. We anticipate that this and related future work will contribute to improve axial accuracy in SMLM to improve 3D reconstructions and gain better insight into biological processes.

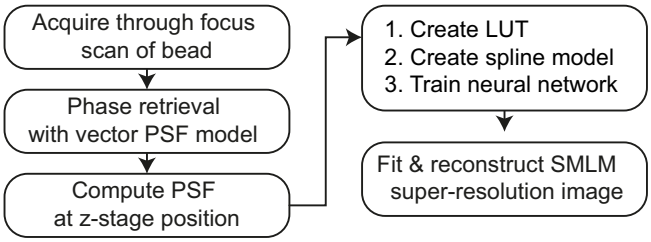

Fig. 6. Proposed workflow for accurate 3D single-molecule localization microscopy with PSF engineering.

Funding. Dutch Research Council, Nederlandse Organisatie voor Wetenschappelijk Onderzoek (NWO), FOM program Neurophotonics.

Acknowledgments. The authors thank Eugene Katrukha for useful discussions and feedback. This work was funded by the Dutch Research Council (NWO) through the FOM program Neurophotonics.

Disclosures. The authors declare no conflicts of interest.

Data availability. The data and code underlying the results presented in this paper are available in Ref. [32].

References

1. E. Betzig, G. H. Patterson, R. Sougrat, O. W. Lindwasser, S. Olenych, J. S. Bonifacino, M. W. Davidson, J. Lippincott-Schwartz, and H. F. Hess, "Imaging intracellular fluorescent proteins at nanometer resolution," Science **313**(5793), 1642–1645 (2006).
2. S. T. Hess, T. P. Girirajan, and M. D. Mason, "Ultra-high resolution imaging by fluorescence photoactivation localization microscopy," Biophys. J. **91**(11), 4258–4272 (2006).
3. M. J. Rust, M. Bates, and X. Zhuang, "Sub-diffraction-limit imaging by stochastic optical reconstruction microscopy (storm)," Nat. Methods **3**(10), 793–796 (2006).
4. B. Huang, W. Wang, M. Bates, and X. Zhuang, "Three-dimensional super-resolution imaging by stochastic optical reconstruction microscopy," Science **319**(5864), 810–813 (2008).

Optics EXPRESS

5. C. Smith, M. Huisman, M. Siemons, D. Grunwald, and S. Stallinga, "Simultaneous measurement of emission color and 3D position of single molecules," Opt. Express **24**(5), 4996–5013 (2016).
6. C. N. Hulleman, R. O. Thorsen, E. Kim, C. Dekker, S. Stallinga, and B. Rieger, "Simultaneous orientation and 3D localization microscopy with a vortex point spread function," Nat. Commun. **12**(1), 5934 (2021).
7. M. P. Backlund, M. D. Lew, A. S. Backer, S. J. Sahl, G. Grover, A. Agrawal, R. Piestun, and W. E. Moerner, "The double-helix point spread function enables precise and accurate measurement of 3D single-molecule localization and orientation," Proc. SPIE **8590**, 85900L (2013).
8. S. Prasad, "Rotating point spread function via pupil-phase engineering," Opt. Lett. **38**(4), 585–587 (2013).
9. C. Roider, A. Jesacher, S. Bernet, and M. Ritsch-Marte, "Axial super-localisation using rotating point spread functions shaped by polarisation-dependent phase modulation," Opt. Express **22**(4), 4029–4037 (2014).
10. Y. Shechtman, S. J. Sahl, A. S. Backer, and W. E. Moerner, "Optimal point spread function design for 3D imaging," Phys. Rev. Lett. **113**(13), 133902 (2014).
11. A. Aristov, B. Lelandais, E. Rensen, and C. Zimmer, "Zola-3D allows flexible 3D localization microscopy over an adjustable axial range," Nat. Commun. **9**(1), 2409 (2018).
12. Y. Li, M. Mund, P. Hoess, J. Deschamps, U. Matti, B. Nijmeijer, V. J. Sabinina, J. Ellenberg, I. Schoen, and J. Ries, "Real-time 3D single-molecule localization using experimental point spread functions," Nat. Methods **15**(5), 367–369 (2018).
13. E. Nehme, D. Freedman, R. Gordon, B. Ferdman, L. E. Weiss, O. Alalouf, T. Naor, R. Orange, T. Michaeli, and Y. Shechtman, "DeepSTORM3D: dense 3D localization microscopy and PSF design by deep learning," Nat. Methods **17**(7), 734–740 (2020).
14. N. Bourg, C. Mayet, G. Dupuis, T. Barroca, P. Bon, S. Lécart, E. Fort, and S. Lévêque-Fort, "Direct optical nanoscopy with axially localized detection," Nat. Photonics **9**(9), 587–593 (2015).
15. C. Cabriel, N. Bourg, P. Jouchet, G. Dupuis, C. Leterrier, A. Baron, M. A. Badet-Denisot, B. Vauzeilles, E. Fort, and S. Lévêque-Fort, "Combining 3D single molecule localization strategies for reproducible bioimaging," Nat. Commun. **10**(1), 1980 (2019).
16. J. Deschamps, M. Mund, and J. Ries, "3D superresolution microscopy by supercritical angle detection," Opt. Express **22**(23), 29081–29091 (2014).
17. P. Kanchanawong, G. Shtengel, A. M. Pasapera, E. B. Ramko, M. W. Davidson, H. F. Hess, and C. M. Waterman, "Nanoscale architecture of integrin-based cell adhesions," Nature **468**(7323), 580–584 (2010).
18. N. Scheefhals and H. D. MacGillavry, "Functional organization of postsynaptic glutamate receptors," Mol. Cell. Neurosci. **91**, 82–94 (2018).
19. M. E. Siemons, N. A. K. Hanemaaijer, M. H. P. Kole, and L. C. Kapitein, "Robust adaptive optics for localization microscopy deep in complex tissue," Nat. Commun. **12**(1), 3407 (2021).
20. M. A. Thompson, M. D. Lew, M. Badieirostami, and W. E. Moerner, "Localizing and tracking single nanoscale emitters in three dimensions with high spatiotemporal resolution using a double-helix point spread function," Nano Lett. **10**(1), 211–218 (2010).
21. D. Fu, J. J. E. Maris, K. Stanciakova, N. Nikolopoulos, O. van der Heijden, L. D. B. Mandemaker, M. E. Siemons, D. Salas Pastene, L. C. Kapitein, F. T. Rabouw, F. Meirer, and B. M. Weckhuysen, "Unravelling Channel Structure-Diffusivity Relationships in Zeolite ZSM-5 at the Single-Molecule Level," Angew. Chem., Int. Ed. **61**(5), e202114388 (2022).
22. B. Huang, S. A. Jones, B. Brandenburg, and X. Zhuang, "Whole-cell 3D storm reveals interactions between cellular structures with nanometer-scale resolution," Nat. Methods **5**(12), 1047–1052 (2008).
23. M. J. Mlodzianoski, P. J. Cheng-Hathaway, S. M. Bemiller, T. J. McCray, S. Liu, D. A. Miller, B. T. Lamb, G. E. Landreth, and F. Huang, "Active psf shaping and adaptive optics enable volumetric localization microscopy through brain sections," Nat. Methods **15**(8), 583–586 (2018).
24. H. Heydarian, M. Joosten, A. Przybylski, F. Schueder, R. Jungmann, B. V. Werkhoven, J. Keller-Findeisen, J. Ries, S. Stallinga, M. Bates, and B. Rieger, "3D particle averaging and detection of macromolecular symmetry in localization microscopy," Nat. Commun. **12**(1), 2847 (2021).
25. Y. Li, Y. L. Wu, P. Hoess, M. Mund, and J. Ries, "Depth-dependent psf calibration and aberration correction for 3D single-molecule localization," Biomed. Opt. Express **10**(6), 2708–2718 (2019).
26. P. N. Petrov and W. E. Moerner, "Addressing systematic errors in axial distance measurements in single-emitter localization microscopy," Opt. Express **28**(13), 18616–18632 (2020).
27. S. Stallinga and B. Rieger, "Accuracy of the Gaussian point spread function model in 2D localization microscopy," Opt. Express **18**(24), 24461–24476 (2010).
28. W. Welford, *Aberrations of Optical Systems* (Hilger, 1986).
29. R. Berlich and S. Stallinga, "High-order-helix point spread functions for monocular three-dimensional imaging with superior aberration robustness," Opt. Express **26**(4), 4873–4891 (2018).
30. S. Ghosh and C. Preza, "Characterization of a three-dimensional double-helix point-spread function for fluorescence microscopy in the presence of spherical aberration," J. Biomed. Opt. **18**(3), 036010 (2013).
31. C. Cabriel, N. Bourg, G. Dupuis, and S. Leveque-Fort, "Aberration-accounting calibration for 3D single-molecule localization microscopy," Opt. Lett. **43**(2), 174–177 (2018).
32. M. E. Siemons, L. C. Kapitein, and S. Stallinga, "On the z-accuracy in 3D single-molecule localization microscopy - supplementary data and code," figshare (2022), https://doi.org/10.6084/m9.figshare.19674732.v1.